POLISH MARITIME RESEARCH 3 (127) 2025 Vol. 32; pp. 118-130
10.2478/pomr-2025-0040

FAULT DIAGNOSIS BASED ON IMPROVED INFORMATION ENTROPY AND 1DCNN FOR MARINE TURBOCHARGER ROTOR WITH VARIABLE SPEED

Lei Hu[1]
Haoran Hu[1]
Nao Hu1*
Luyuan Liu[1]
Fei Dong[1]
Jianguo Yang[1]
Jiahong Zhong[2]

[1] Wuhan University of Technology, School of Naval Architecture, Ocean and Energy Power Engineering, Wuhan, China
[2] Chongqing Jiangjin Shipbuilding Industry Co., Ltd, China

* Corresponding author: *nao.hu@whut.edu.cn (Nao Hu)*

ABSTRACT

Due to the lack of a standardised method for determining representative locations for measuring points, it is difficult to select sensitive data on turbocharger rotor faults. In addition, the uncertainty in the feature parameters used for diagnosis under variable rotational speeds leads to low accuracy in fault identification. To address these issues, vibration signals from a turbocharger rotor under various conditions are obtained in this study via a fault simulation test, and a fault diagnosis method for rotor faults under variable speed conditions is proposed based on a sensitivity and multi-dimensional feature analysis of measurement points. The sensitivity of the improved and traditional information entropy is evaluated using a variance analysis across the measurement points, and the most effective vibration measurement points are selected based on the improved information entropy. The effective characteristic parameters of the vibration signals at multiple measurement points are analysed and extracted, and the number of dimensions of the feature parameters is reduced using the t-distributed stochastic neighbour embedding (t-SNE) method. Faults in the turbocharger rotor at the different speeds are classified using a one-dimensional convolutional neural network (1DCNN), and the arithmetic ability of the diagnostic algorithm is evaluated. The results demonstrate that the proposed methods of selecting measurement points and fault diagnosis can effectively identify rotor faults at different degrees and various speeds: the accuracy of fault diagnosis is 99.85%, and the arithmetic ability is markedly enhanced compared with that of traditional methods.

Keywords: marine turbocharger; sensitivity analysis; variable speed; improved information entropy; feature fusion

INTRODUCTION

When used in a marine engine, a turbocharger can make effective use of the energy from the outlet gases, which improves thermal efficiency and significantly enhances power [1–3]; these devices therefore play a crucial role in ensuring that diesel engines can provide the continuous and stable power required for ship navigation, as well as reducing the environmental impact of exhaust emissions [4,5], and are widely used in marine power systems. However, turbochargers are used under harsh conditions, including unpredictable events (such as high rotational speeds), variable operating conditions, stringent lubrication requirements, variation in the thermal load of the engine, and quickly changing temperatures of exhaust gases, among others [6,7]. These factors may induce rotor imbalance in a turbocharger through multiple mechanisms, such as impact damage to the compressor blades caused by object ingestion, and striking damage to the turbine blades resulting from engine carbon deposits. These modes of failure may also interact synergistically, resulting in an asymmetric mass distribution of the rotor. It is therefore important to study fault diagnosis methods for a turbocharger rotor under variable and high-speed conditions, to ensure the stable operation of marine engines.

Fault diagnosis methods for rotating machinery mainly rely on model-based and data-driven approaches. Data-driven fault diagnosis offers high accuracy, and enables real-time detection through the acquisition of vibration signals from sensors. Many of the current fault diagnosis methods are therefore data-driven, based on vibration signals, and a data-driven diagnostic methodology is adopted in this study [8]. Methods based on support vector machine (SVM) [9–11], Pearson correlation coefficients, long short-term memory (LSTM) networks [12], BP neural networks [13] and wavelet analysis [14,15] have been used for theoretical analysis and experimental verification of fault diagnosis; however, in these studies, signals have been obtained from a single measurement point, or information on one or more of the X-, Y-, and Z-directions is lacking, leading to the loss of valuable data and reduced diagnosis accuracy. To address the issue of the limited information contained in signals from single points, data-layer fusion of signals from multiple measurement points has been studied by Qiao Jingguo [16] and Xu Wangmin [17]. This method enables signals from various measurement points to be fully used, thereby improving the accuracy of fault diagnosis. However, fusion of all measurement points at the data layer requires extended processing times, which degrades real-time data processing performance, while real-time capability is crucial for the online diagnosis of marine power systems [18]. Furthermore, the inclusion of invalid or redundant information from some measurement points cannot be prevented [19,20].

Moreover, the studies described above have not considered the impact of speed variations on diagnostic results. Since the rotational speed of a turbocharger varies significantly with fluctuations in engine load, the robustness of fault diagnosis methods across diverse speed conditions is critical [21,22]. Hence, the adaptability of these methods to variable-speed operating conditions cannot be verified. To address this issue, Fei Dong et al. [23,24] used time-frequency analysis and TrAdaBoost transfer learning methods to carry out fault diagnosis for a marine turbocharger at multiple speeds based on vibration signals. Qiao Qi et al. [25] used Desnet-ViT joint network transfer learning to generate a model for rotor fault diagnosis under variable-speed operating conditions, in which the network was trained on motor bearing signals. Both methods achieved good diagnostic results. However, the primary objective of transfer learning is to reduce the training time for the model. When transfer learning is used for fault diagnosis under variable speed conditions, the classifier model still requires a small amount of data from the target domain for re-training. In real-time fault diagnosis processes, training the model on the target domain data at the current rotational speed is time-consuming. Consequently, the method described above is not adaptable to real-time fault diagnosis under variable speed conditions. It is therefore necessary to propose a diagnosis method for turbocharger rotor faults with the characteristics of short time consumption, high accuracy and adaptability to variable speeds.

Tab. 1. List of abbreviations

IIE	Improved information entropy
TIE	Traditional information entropy
PCA	Principal component analysis
KPCA	Kernel principal component analysis
t-SNE	t-distributed stochastic neighbour embedding
1DCNN	One-dimensional convolutional neural network
DPT	Data processing time after selecting the measurement points
DPT_S	Data processing time using all measurement points
RAMO	Random access memory occupation
CR	Complex rate
EMD	Empirical mode decomposition
IMF	Intrinsic mode function of VMD
k	Number of VMD modal components
u_k	Modal function of VMD
ω_k	Central frequency of μ_k
∂_t	Partial derivative with respect to time
$\delta(t)$	Dirac function
E_i	Event of information entropy of the th IMF component
x_{ij}	Value of the th frequency-domain signal data point in the th IMF component
f_{ij}	Frequency value corresponding to x_{ij}
H_v	IIE under one of the rotational speed categories
H_w	Value of IIE under all rotational speeds
H_{wa}	IIE of one of the fault states under all rotational speeds
H_i	Final IIE of one of the measurement points
$\overline{H}$	Average value of IIE for all measurement points
SE	Sensitivity of IIE for all measurement points
x_i	th data point in the time series signal
μ	Average value of the time series signal
σ	Standard deviation of the time series signal
P	Amplitude of each spectral line of the time series signal spectrum
f	Frequency corresponding to P
$S1$	Centre of gravity frequency
$S2$	Mean square frequency
y	Output of the convolutional layer of 1DCNN
$x_i^{(l-1)}$	Output of the th convolutional kernel of the l–1th layer
$k_{ij}^{(l-l)}$	Weight between the ith and j^{th} neurons of the l^{th} layer

METHOD AND FLOW OF FAULT DIAGNOSIS

In this study, a turbocharger rotor fault simulation experiment was conducted. Vibration measurement points were arranged at multiple positions and directions on the turbocharger test bench to collect signals from various parts of the turbocharger. Since the signals acquired from different measurement points have varying levels of diagnostic relevance, the selection of sensitive measurement points is essential in order to optimise the fault detection accuracy. To address this, an improved information entropy (IIE) method is proposed, which enables systematic identification of sensitive measurement points through a comparative analysis of IIE values.

Next, the trends of vibration signal feature parameters were analysed. Parameters demonstrating strong discriminative capabilities across varying rotational speeds were selected from the measurement points to construct a high-dimensional feature vector for fault characterisation.

Finally, dimensionality reduction was performed on the feature vector using the t-SNE method. The reduced feature vector was subsequently employed for fault diagnosis via a 1D convolutional neural network (1DCNN).

The overall flowchart of fault diagnosis in the paper is shown in Fig. 1.

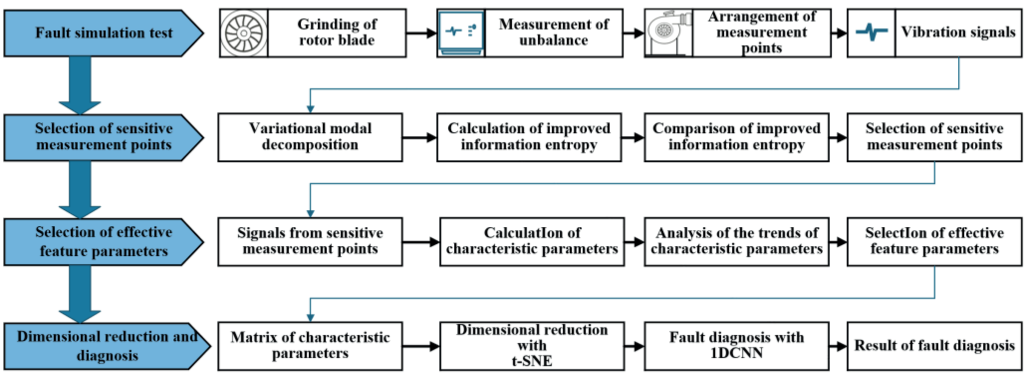

Fig. 1. Flowchart of the process

PROPOSED IIE METHOD

INFORMATION ENTROPY

Information entropy is a statistical value that represents the amount of information contained in a signal: the greater the information entropy, the greater the amount of information contained in the signal [0. There are many methods for calculating the information entropy. One of the most widely used involves first converting time-domain signals into frequency-domain signals via Fourier transform, and then calculating the information entropy from the frequency-domain signals.

Before calculating the information entropy, it is necessary to decompose the signal to compute the entropy characteristics of the decomposed signals for each order. The most commonly used signal decomposition methods include empirical modal decomposition (EMD), ensemble EMD (EEMD) and variational mode decomposition (VMD). As an improved version of the EMD algorithm, EEMD can solve the mode aliasing problem that arises with the EMD method to a certain extent, and many fault diagnosis studies based on the EEMD method have achieved good results. However, if the noise amplitude is not chosen properly, it may lead to instability in the EEMD results or introduce additional errors [29]. Under the high-speed operational conditions of a turbocharger and the significant background noise in the vibration signals, the VMD method yields superior anti-aliasing and noise suppression performance compared to the EMD and EEMD methods [30,31]. This enhanced capability makes it particularly suitable for processing turbocharger vibration signals in noise-intensive environments. The VMD constrained variational model is shown in Eq. (1).

$$\min_{\{u_k\},\{\omega_k\}} \left\{ \sum_k \left\| \partial_t \left[\left(\delta(t) + (j/\pi t) \right) * u_k(t) \right] e^{-j\omega_k t} \right\|_2^2 \right\}, \ s.t. \sum_k u_k = f \quad \textbf{(1)}$$

where u_k is the modal function, ω_k is the centre frequency of u_k, ∂_t is the partial derivative with respect to time t, $\delta(t)$ is the Dirac function, and $(j/\pi t)$ is the Hilbert transform operator. If the vibration signal f of the turbocharger is decomposed into k modal components, it is necessary to ensure that the decomposition sequence is a finite bandwidth modal component with a centre frequency, while the sum of the estimated bandwidths for each mode is minimised, and the constraint is that the sum of all the modes is equal to that of the original signal.

Fig. 2 shows the spectra for the selected modal components (levels 4–6) at the minimum rotational speed (35,000 rpm) and maximum speed (60,000 rpm). It can be seen that the sixth modal component contains critical frequency components such as the fundamental frequency and harmonics across both speed ranges, while the fourth modal component effectively confines the signal frequency to approximately 12.8 kHz, ensuring that the reconstructed signal remains within the measurable frequency range of the sensor.

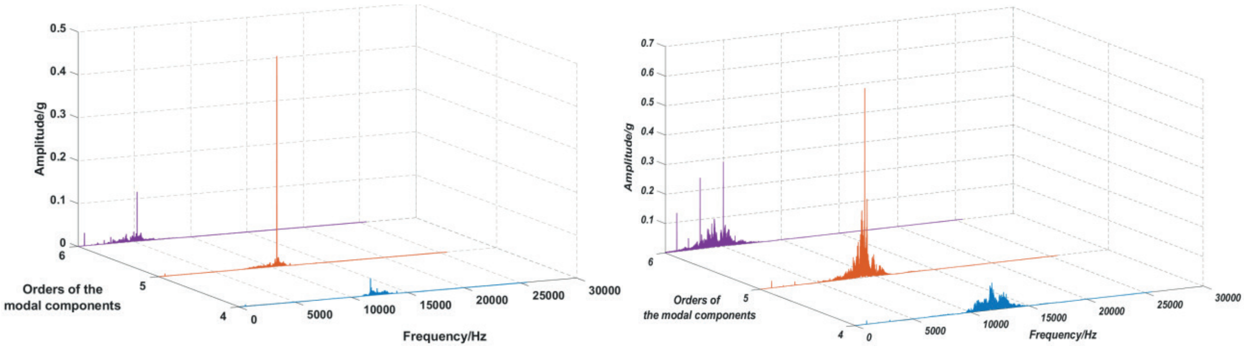

(a) 35,000 rpm *(b) 60,000 rpm*

Fig. 2. Results from VMD

IMPROVED INFORMATION ENTROPY

Information entropy is typically used as a characteristic parameter of vibration signals, and is not considered as an indicator for evaluating the amount of information contained at measurement points [29]. In addition, when calculating the traditional frequency-domain information entropy (TIE), the probability of events only contains the amplitude of the energy. For a turbocharger under variable rotational speed conditions and a multi-bladed structure at the compressor and turbine, attention should also be paid to the frequency characteristics, such as the fundamental frequency, the octave frequency and its side frequency. In view of this, the IIE calculation method is modified by updating the definition of an event E from Eq. (2) to that in Eq. (3). In addition, to avoid randomness in the information entropy across different rotational speeds and measurement points, the information entropy of the different rotational speeds is summed and then averaged over all fault states, as shown in Eqs. (4) and (5). The spectra for some signals are shown in Fig. 3, with certain features such as the fundamental frequency and harmonics.

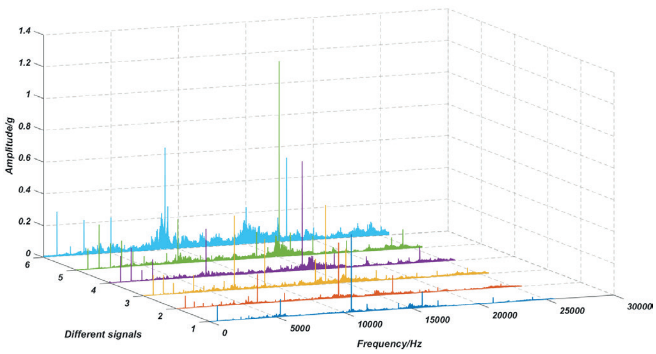

Fig. 3. Spectra for some signals

$$E_i = \sum_{j=1}^{n}(x_{ij}{}^2) \quad (2)$$

$$E_i = \sum_{j=1}^{n}(x_{ij} * f_{ij}) \quad (3)$$

where j is the number of data points of the frequency-domain signal, x_{ij} is the value of the j^{th} frequency-domain signal data point in the i^{th} IMF component, and f_{ij} is the frequency value corresponding to x_{ij}.

$$H_w = \sum_{k=1}^{m} H_v \quad (4)$$

where v is the number of rotational speed categories (if the acquired signal contains m different speeds, the value of v ranges from 1 to m), and H_w is the value of the IIE under all rotational speeds.

$$H_c = \frac{H_{w1}+H_{w2}+\cdots+H_{wa}}{a} \quad (5)$$

where c is the number of the measuring points, H_{wa} is the IIE of one of the fault states under all rotational speeds, a is the number of fault states, and H_c is the value of IIE which is finally needed of the cth measurement point.

SIMULATION EXPERIMENT AND SENSITIVE FEATURES OF THE ROTOR

EXPERIMENTAL DESIGN AND DATASET ACQUISITION

The rotor fault simulation test was carried out using a marine turbocharger test bench. The rotor was first polished to adjust the edge mass, in order to simulate various degrees of imbalance, and the value of the rotor imbalance was measured with a dynamic balancing machine. The configuration of the rotor imbalance test bench is shown in Fig. 4, and the different degrees of rotor imbalance fault are defined in Table 2. To reflect the operational lifecycle of a turbocharger, a slight imbalance is defined as an early-stage fault of the rotor, while a severe imbalance is classified as a late-stage fault. Turbocharger rotors with different degrees of imbalance were installed in the machine to carry out fault simulation tests. To avoid a high temperature near the turbocharger shell, eight measurement points were arranged at different locations near the bearing and foot of the turbocharger, with specific locations and directions as shown in Fig. 5 and Table 3. The hot exhaust gases generated by a diesel combustion chamber were used as the power input to the turbocharger. The vibration signals were collected with B&K 4534B accelerometers and a Siemens Simcenter SCADAS Mobile acquisition system, and the test conditions and sampling parameters are shown in Table 4.

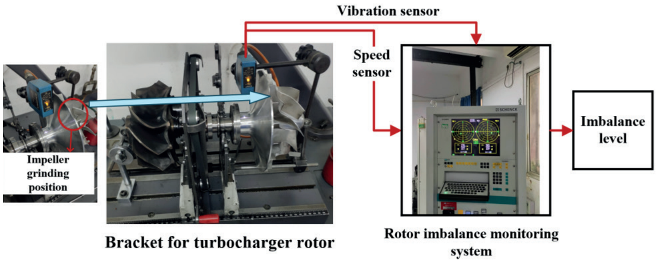

Fig. 4. Composition of the rotor imbalance test bench

Tab. 2. Degree of rotor imbalance and corresponding fault

Imbalance /g*mm	Degree of fault
3.4	Normal
7.6	Minor imbalance
10	Severe imbalance

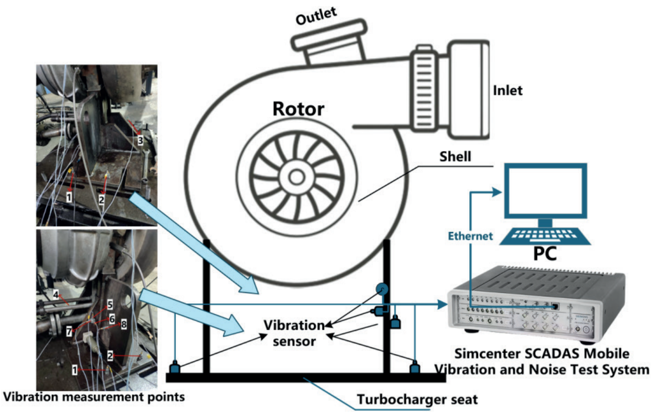

Fig. 5. Layout of the signal acquisition system and measurement points

Tab. 3. Locations of the different measurement points

Number	Direction	Location
1	Z	Vertical direction of the foot on the compressor side
2	Z	Vertical direction of the foot on the turbine side
3	Z	Vertical direction of the foot on the turbine side
4	Z	Vertical direction of the foot on the compressor side
5	Z	Vertical direction of the bracket on the compressor side
6	Y	Vertical to the rotor axle on the compressor side
7	X	Rotor axial direction on the compressor side
8	X	Rotor axial direction on the compressor side

Tab. 4. Test conditions and settings of sampling parameters

Speed/rpm	State of rotor	Length of signal /s	Sampling rate /kHz
35,000–60,000 (steps of 2,500 rpm)	Degree 1: Normal Degree 2: Minor imbalance Degree 3: Severe imbalance	5	51.2

During signal processing, it was found that some values of the time domain signals appeared to deviate from the normal range. Abnormal data values were removed using the 3σ criterion, the principle of which is shown in Eq. (6). If the sample was larger than μ + 3σ or smaller than μ–3σ, it was judged to be abnormal, and was removed to ensure the validity of the dataset.

$$|x_i - \mu| > 3\sigma \quad \textbf{(6)}$$

where x_i represents the ith data point, μ is the average of the samples, and σ is the standard deviation of the samples

SENSITIVITY ANALYSIS AND SELECTION OF THE MEASUREMENT POINTS

Prior researchers have explored various methodologies for the selection of measurement points. Methods such as the analysis of amplitude transmission patterns of vibration signals [32], dimensionality reduction of feature parameters [33], and modal analysis [34] have been employed for the optimisation and screening of measurement points.When used together, these techniques can enhance the identification of sensor locations with maximal diagnostic relevance while minimising the acquisition of redundant data.

A comparison of the calculated results for the IIE and TIE at each measurement point based on Eqs. (3)–(5) is shown on the left axis of Fig. 6. To avoid the excessive differences affecting the subsequent judgment between the values of two entropy TIE and IIE, the mean values of the two entropies were deducted for normalisation processing to eliminate the difference in amplitude while retaining the fluctuation. The sensitivity (was calculated to determine the sensitivity of the entropy value for each the measurement points. The value of for the IIE is calculated according to Eq. (7):

$$SE = \frac{\sum_{i=1}^{n}(H_i - \bar{H})^2}{n} \quad (7)$$

where H_i is the IIE of each measurement point, and $\bar{H}$ is the average value of IIE.

A large SE for the entropy value indicates a significant fluctuation at the measurement point, thereby demonstrating a high sensitivity of the entropy. The results shown on the right axis of Fig. 6 indicate that the SE for the IIE is significantly larger than for the TIE. When the IIE is used to measure the amount of information contained in the signal, it is more sensitive to a change in the measurement points, meaning that it is better than the TIE.

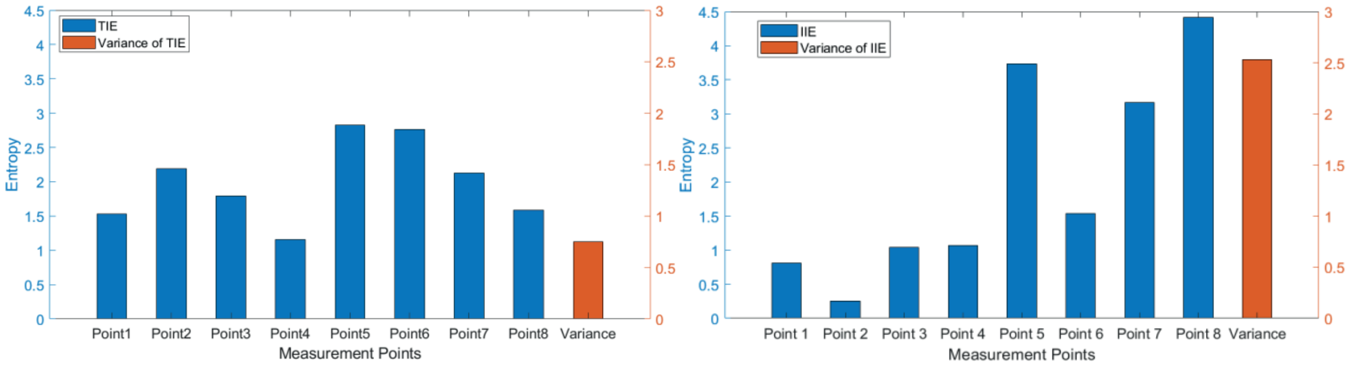

(a) TIE *(b) IIE*

Fig. 6. Sensitivity analysis of entropy values at different measuring points

From Fig. 6, it can be seen that points 5, 6, 7, and 8 are unambiguously identified as sensitive measurement points for the improved entropy. In contrast, when using the TIE method, it is difficult to distinguish between measurement points 2 and 7, as well as between points 5 and 6, because the entropy values for these two pairs of points are very close. Selecting all such points would introduce redundant or invalid data, potentially compromising the diagnostic efficacy. The improved method eliminates this ambiguity, ensuring a precise and reliable selection of measurement points for enhanced fault diagnosis performance. Hence, points 5, 6, 7 and 8 are taken as sensitive measurement points.

Based on the selection results at these measurement points using IIE and the arrangement of the points shown in Fig. 5, it can be observed that measurement points 5, 6, 7, and 8, which are identified as sensitive measurement points, are located close to the turbocharger body and cover all directions (X, Y, and Z). Measurement points 1, 2, 3, and 4, with low IIE, are located not only at the foot position, which is farther from the turbocharger, but also in the single Z-direction. Consequently, the proposed selection method based on IIE provides the following guidance: measurement points should be located close to the object to be measured, and should include the X-, Y-, and Z-directions.

SELECTION OF EFFECTIVE FEATURE PARAMETERS

When selecting feature parameters, the following criteria should be met: the curve of the fluctuations of the feature parameters with speed should be flat, and the feature parameters should clearly distinguish between different degrees of imbalance fault at each speed. Based on the above criteria, the centre of gravity frequency and the mean square frequency are chosen as effective feature parameters, and the methods used to calculate them are shown in Eqs. (8) and (9):

Centre of gravity frequency:

$$S1 = \frac{\sum_1^n (P*f)}{\sum_1^n P} \tag{8}$$

Mean square frequency:

$$S2 = \frac{\sum_1^n (P*f^2)}{\sum_1^n P} \tag{9}$$

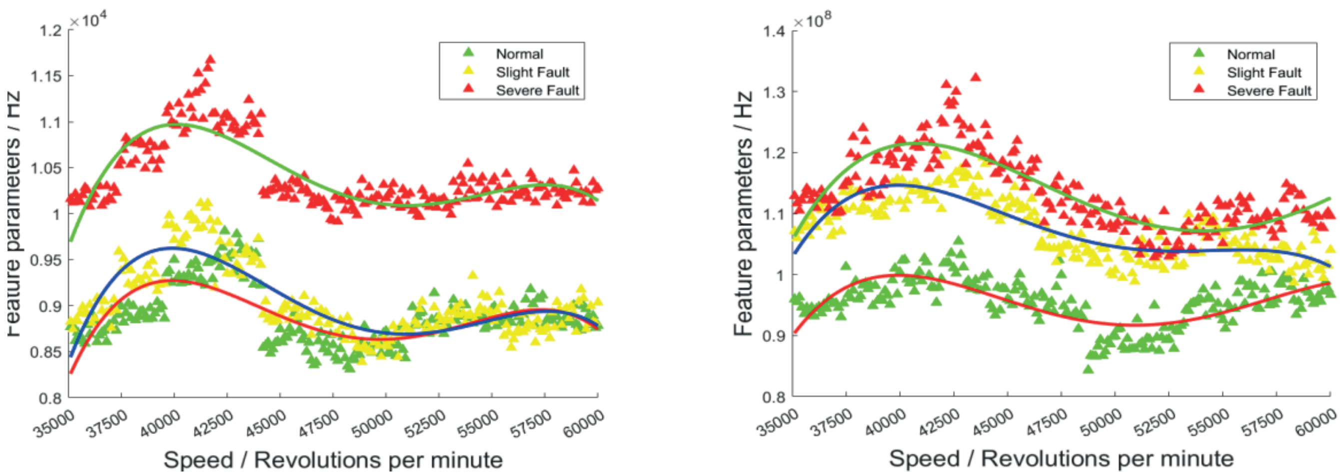

(a) Changes in feature parameter S1 *(b) Changes in feature parameter S2*

Fig. 7. Changes in the feature parameters for S1and S2 at different speeds

where P is the amplitude of each spectral line of the signal spectrum, f is the frequency corresponding to the amplitude of each spectral line, and n is the number of spectral lines. The variations in the centre of gravity frequency and mean square frequency with speed are shown in Fig. 7.

The curves for the two selected feature parameters show flat behaviour at different speeds, and the three degrees of rotor imbalance fault can be clearly distinguished. Feature parameter S1 has a significant advantage in terms of distinguishing Degree 3 from the other two types of faults, but the trend lines of Degree 1 and Degree 2 overlap in the high-speed range, resulting in poor discrimination. Feature parameter S2 has a clear advantage in regard to distinguishing Degree 1 from the other two types of faults, but the difference is not large between the different fault degrees, especially for Degrees 2 and 3, which may have an impact on the fault identification accuracy. Hence, a fault recognition method that combines these two feature parameters may improve the accuracy of fault diagnosis, and may demonstrate good fault recognition performance at high speeds when identifying these three degrees of faults.

MULTI-POINT FEATURE FUSION AND DIMENSION REDUCTION

Multi-point feature fusion based on eight dimensions is carried out using effective feature parameters from measurement points 5, 6, 7 and 8. Direct use of a high-dimensional fusion vector for fault diagnosis could lead to excessive amounts of computation and reduced algorithm efficiency, resulting in excessive redundant information or dimensional catastrophe. It is therefore necessary to perform dimension reduction on the high-dimensional feature vector to minimise redundancy and preserve the fault information for the marine turbocharger rotor.

The most commonly used algorithms for dimension reduction of high-dimensional data are principal component analysis (PCA), kernel PCA (KPCA) and t-SNE. PCA is a widely used method for linear dimensionality reduction [35–37], which is achieved by finding the directions of maximum variance (principal components) in the data and projecting the data onto these directions. KPCA, an improved nonlinear version of PCA, is a kernel-based dimensionality reduction algorithm [38] that deals with nonlinear data by using kernel functions to map the data to a high-dimensional space and then performing PCA in the high-dimensional space. t-SNE is a nonlinear manifold learning dimensionality reduction algorithm, and achieves dimensional reduction by converting the similarity between high-dimensional data points to t-distributions in low-dimensional space and then minimising the differences between the distributions [39–41]. Fig. 8 shows a comparison of the visualisation results after reducing the eight-dimensional vector feature of the rotor fault simulation test data to three dimensions using PCA, KPCA and t-SNE.

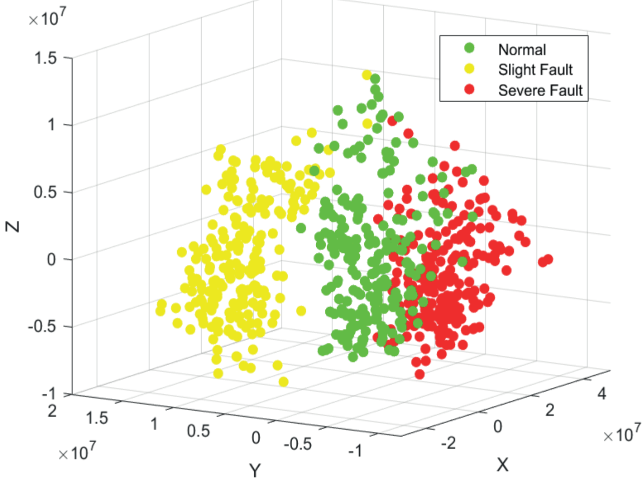

(a) Dimension reduction with the PCA method

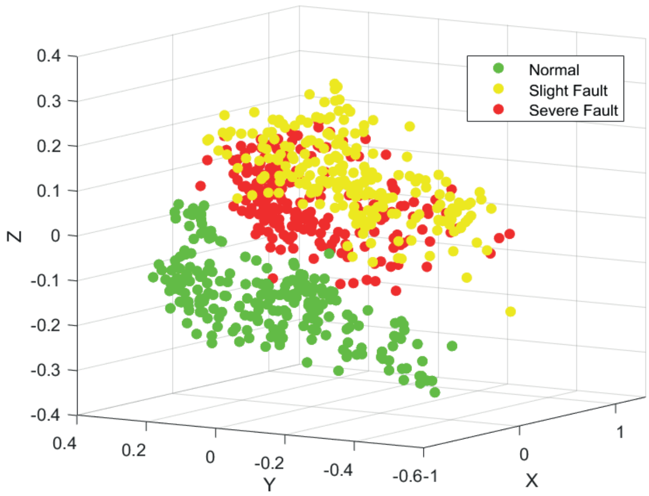

(b) Dimension reduction with the KPCA method

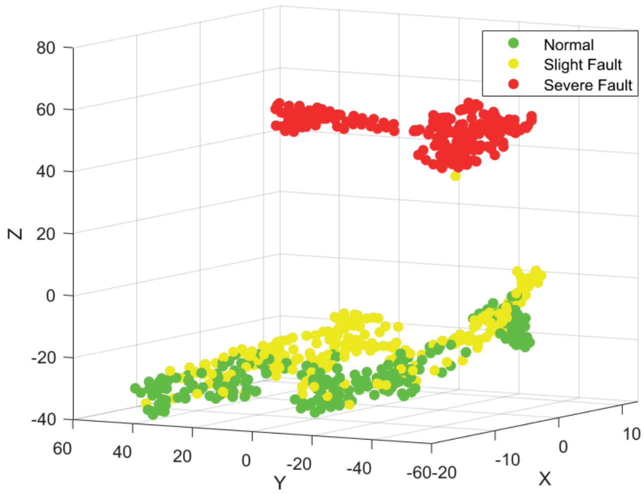

(c) Dimension reduction with the t-SNE method for S1

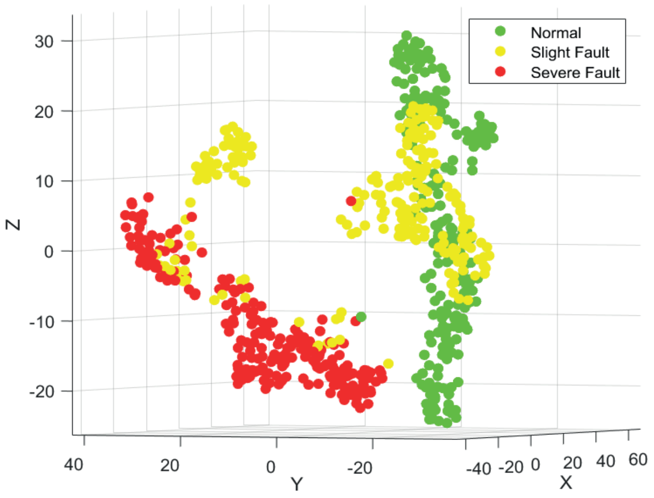

(d) Dimension reduction with the t-SNE method for S2

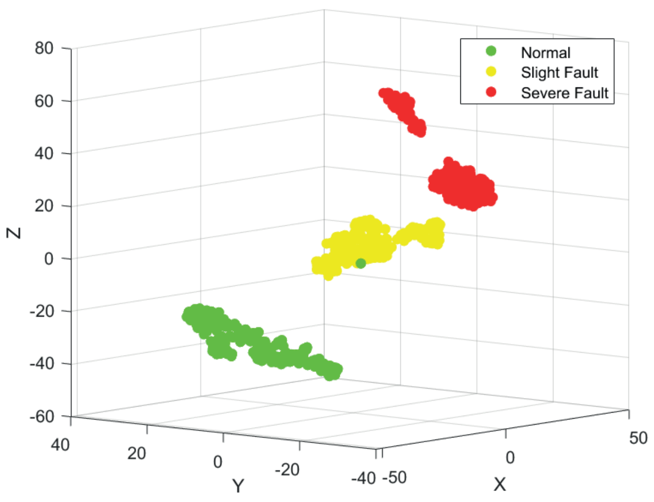

(e) Dimension reduction with the t-SNE method for S1 and S2

Fig. 8. Visual comparison of the effects of different dimensional reduction methods

From Fig. 8(e), it can be observed that the three types of data are clearly separated, with significant space between each category, after applying t-SNE, which is superior to the PCA and KPCA methods. In addition, from Figs. 8(c) to (e), it is evident that using two effective feature parameters, S1 and S2, for dimensional reduction gives far better results than using a single feature parameter. This confirms that the two selected feature parameters achieve superior fault discrimination results through multi-feature fusion.

FAULT DIAGNOSIS BASED ON 1DCNN

A one-dimensional convolutional neural network (1DCNN) is a deep feed-forward artificial neural network [42] whose main structure consists of an input layer, a convolutional layer, a pooling layer, a fully connected layer and an output layer [43]. 1DCNN is capable of deeply exploring the time-varying features in variable speed signals; it effectively captures the high-frequency features, reduces the complexity, and improves the diagnosis efficiency through pooling operations. Hence, 1DCNN is a superior method for the fault diagnosis of a turbocharger rotor at high rotational speeds in noisy environments, where vibration signals exhibit complex, high-dimensional fault features. The structure and configuration of the 1DCNN are shown in Fig. 9 and Table 5, and the output of the convolutional layer is shown in Eq. (10).

$$y_j^l = f\left(b_j^l + \sum\nolimits_{i\in M_j} conv\left(x_i^{l-1}, k_{ij}^{l-1}\right)\right) \quad (10)$$

where y represents the jth output of the lth layer, f is a nonlinear function, b is the bias of the jth neuron of the lth layer, x_i^{l-1} is the output of the ith convolutional kernel of the l–1[th] layer, and k represents the weight between the ith and jth neurons of the lth layer. The input to the 1DCNN considered in this paper is the feature vector after being reduced to three dimensions, and the output is categorised into three levels of fault information: normal, slight fault and severe fault.

Tab.. 5. Configuration of the 1DCNN

Input layer	Feature vectors of signals (3×1)
Feature extractor	Convolution with kernel = 10; ReLU; maxPooling1d (2); Batch norm (256)
Classifier	Fully connected layer (10)
	SoftMax layer
	Output (3×1)

DIVISION OF TRAINING AND TEST SETS

In the process of variable speed fault diagnosis, despite ensuring data accuracy with the 3σ principle, unstable fault characteristics may persist under variable speed conditions, which could lead to reduced accuracy when the same model is applied. The effectiveness of fault diagnosis can be examined using multifold cross-validation, where data for untrained speeds are used as model inputs. Eleven-fold cross-validation

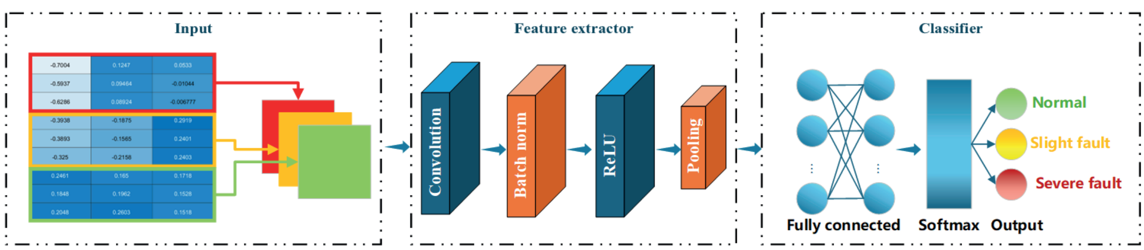

Fig. 9. Structure of the 1DCNN

means that of the 11 possible speeds, the data on 10 of them are used as the training set at each iteration, and the data on the remaining speed are used as the test set. This process is repeated until all data on all 11 speeds have been used as the test set in turn, as shown in Fig. 10.

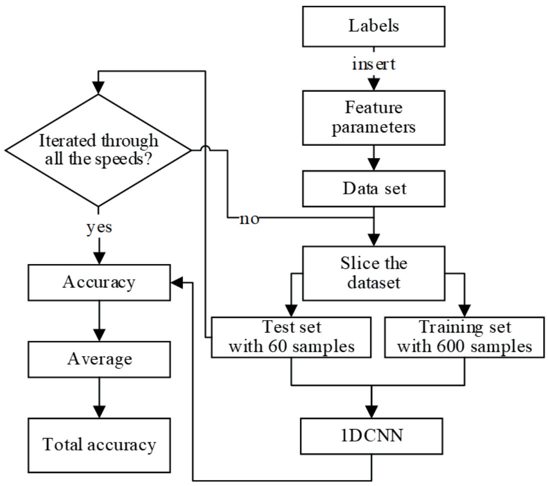

Fig. 10. Flowchart showing training and testing using 11-fold cross-validation

COMPARISON OF FAULT DIAGNOSIS RESULTS

Comparison of fault diagnosis effect

Fig. 11 shows confusion matrices for the fault diagnosis of a turbocharger rotor at different 11 speeds, using the method based on IIE.

It can be seen from Fig. 9 that the proposed fault diagnosis method for a turbocharger rotor based on IIE achieves accuracies higher than 98% for speeds of 35,000 rpm to 60,000 rpm.

Table 6 shows an accuracy comparison for fault diagnosis based on different methods.

Tab. 6. Accuracy comparison for three methods

Speed/ rpm	Method based on IIE		Method based on TIE		Without selection of measurement points	
	Accuracy (%)	Average accuracy (%)	Accuracy (%)	Average accuracy (%)	Accuracy (%)	Average accuracy (%)
35,000	100	99.85	100	86.51	100	99.85
40,000	98.33		100		100	
42,500	100		100		100	
45,000	100		73.33		100	
47,500	100		90		100	
50,000	100		91.67		100	
52,500	100		98.33		100	
55,000	100		100		100	
57,500	100		98.33		98.33	
60,000	100		100		100	

As can be seen from Table 6, the average accuracy based on IIE does not decrease when half of the measurement points are selected, a finding that verifies the effectiveness of the selection method for the measurement points. The fault diagnosis accuracy under variable speed conditions is increased by 15.5% compared to the TIE method.

Comparison of arithmetic ability

Although the fault diagnosis results based on all measurement points are consistent with the accuracy of the IIE method, there are drawbacks, such as the high computer resource consumption due to the large amounts of data processing involved; this leads to high memory requirements for calculation and storage, which are not conducive to the development of engineering applications using online monitoring and fault diagnosis methods for marine turbocharger rotors. To compare the efficiency of the arithmetic ability between the IIE algorithm with selected measuring points and the algorithm with all of the points, we consider three evaluation parameters: data processing time (DPT), random access memory occupation (RAMO) and complex rate (CR). The experiments used a computer configuration with i7 - 13700 CPU, 16G RAM and an ASUS B760 motherboard. The CR value for the IEE method as compared to the algorithm using all of the measurement points is calculated as shown in Eq. (11) [44]. If the value of CR is less than 1, this indicates that the efficiency of the algorithm is higher after selection of the measurement points.

$$CR = \frac{DPT}{DPT_S} \tag{11}$$

where DPT is the data processing time for the algorithm using the measurement points which are selected, and DPT_S is the data processing time for the algorithm using all the measurement points without selection.

Table 7 shows the DPT, RAMO and CR results for fault diagnosis with the two methods.

Tab.. 7. Comparison of parameters for arithmetic evaluation

Method / Parameter	All measurement points	IEE method	Percentage decline
DPT /s	16.95	5.51	207.6%
RAMO /MB	235.5	102.4	130.0%
CR	1.00	0.32	212.5%

Table 7 indicates that the use of the IIE algorithm for selecting measurement points results in a 207.6% reduction in DPT, a 130.0% reduction in memory occupation and a 212.5% reduction in CR. This shows that the efficiency of the proposed fault diagnosis algorithm based on IIE is significantly enhanced.

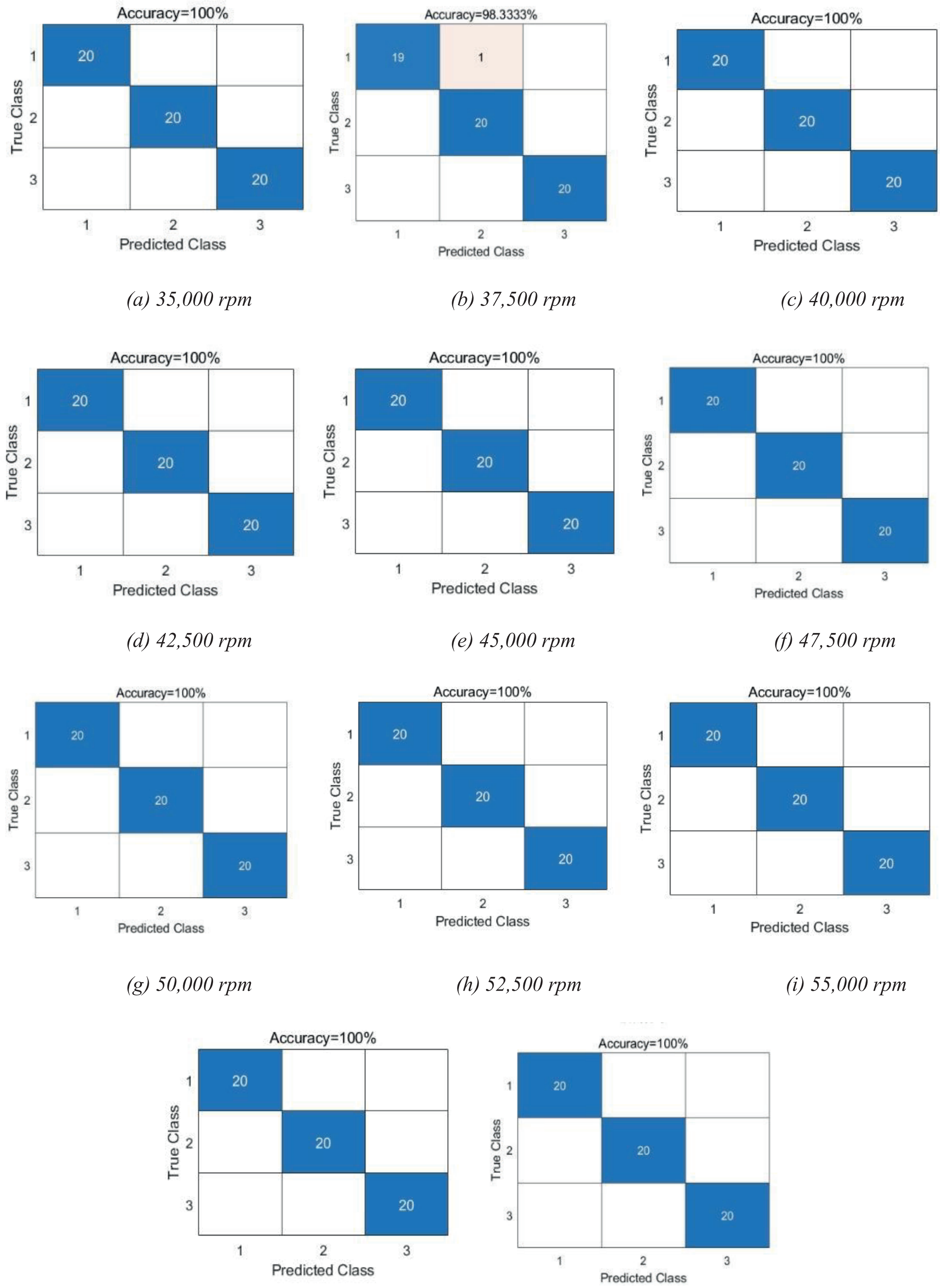

(a) 35,000 rpm (b) 37,500 rpm (c) 40,000 rpm

(d) 42,500 rpm (e) 45,000 rpm (f) 47,500 rpm

(g) 50,000 rpm (h) 52,500 rpm (i) 55,000 rpm

(j) 57,500 rpm (k) 60,000 rpm

Fig. 11. Fault diagnosis confusion matrices for 11 speeds

CONCLUSION

A set of fault experiments on marine turbocharger rotors were carried out, and the IIE method was proposed for the selection of measuring points. The t-SNE method was used for data processing and classification of the optimised measuring points, and a 1DCNN was applied to the task of fault identification of rotors with different speeds. The arithmetic ability of two diagnostic algorithms based on IIE and 1DCNN was compared and evaluated. A suitable diagnostic capability for both early-stage faults, such as slight rotor imbalance, and late-stage faults, such as severe rotor imbalance, in a turbocharger was successfully achieved.

The main conclusions of this work are as follows:

(1) The IIE method was developed, which has considerable advantages in terms of the optimisation of criteria points and extraction of useful features of measurement point signals, reducing the number of sensors, which could significantly reduce the cost of experiment.

(2) Two effective feature parameters of the turbocharger vibration signals under variable speed conditions, referred to here as S1 and S2, were proposed. S1 performed well in classifying rotor faults at low and medium frequencies, but had weak recognition capabilities in the early stages of fault detection. S2 performed well in classifying rotor faults at medium and high frequencies, but had poor recognition performance in the later stages of the fault.

(3) The proposed diagnosis algorithm based on t-SNE and 1DCNN yielded a superior diagnosis capability for rotor imbalance faults under different speeds. Compared to traditional methods, the average fault diagnosis accuracy increased from 86.51% to 99.85%.

(4) The arithmetic ability of the diagnosis algorithm based on IIE and 1DCNN gave significant increases in the evaluation parameters, with the DPT, RAMO and CR rising by 207.6%, 30.7% and 212.5%, respectively. This approach will therefore be beneficial for the development and application of an online fault diagnosis system for marine turbochargers.

ACKNOWLEDGMENTS

This work was supported through a project entitled 'Research and development of high flow and reliability turbocharger for marine low-speed engine', and the experiments were done with a turbocharger test bench at Chongqing Jiangzeng Shipbuilding Heavy Industry Co.

REFERENCES

1. Adamkiewicz A, Nikończuk P. An attempt at applying machine learning in diagnosing marine ship engine turbochargers. Eksploat. Niezawodn. 2022, vol. 24, no. 4, pp. 795–804. https://doi.org/10.17531/ein.2022.4.19

2. Nyongesa AJ, Park MH, Lee CM, et al. Experimental evaluation of the significance of scheduled turbocharger reconditioning on marine diesel engine efficiency and exhaust gas emissions. Ain. Shams. E. J. 2024, vol. 15, no. 8, p. 102845. https://doi.org/10.1016/j.asej.2024.102845

3. Liu M, Yao MF, Wang H. Optimized design and simulation of thermal efficiency of diesel engine based on combustion chamber and turbocharger matching. Internal Combustion Engineering 2021, vol. 42, no. 05, pp. 14–22. DOI: 10.13949/j.cnki.nrjgc.2021.05.003

4. Barelli L, Bidini G, Bonucci F. Diagnosis methodology for the turbocharger groups installed on a 1 MW internal combustion engine. Appl Energ 2009, vol. 86, no. 12, pp. 2721–2730. https://doi.org/10.1016/j.apenergy.2009.04.034

5. Aretakis N, Mathioudakis K, Kefalakis M, et al. Turbocharger unstable operation diagnosis using vibroacoustic measurements. J. Eng. Gas Turbines Power 2004, vol. 126, no. 4, pp. 840–847. https://doi.org/10.1115/1.1771686

6. Girtler J, Rudnicki J. Quantumness in diagnostics of marine internal combustion engines and other ship power plant machines. Pol Marit Res 2023 vol. 4, pp. 110–119. https://doi.org/10.2478/pomr-2023-0064

7. Puzdrowska P. Diagnostic information analysis of quickly changing temperature of exhaust gas from marine diesel engine. Part I: Single factor analysis. Pol Marit Res 2021, vol. 4, pp. 97–106. https://doi.org/10.2478/pomr-2021-0052

8. Varbanets R, Shumylo O, Marchenko A, et al. Concept of vibroacoustic diagnostics of the fuel injection and electronic cylinder lubrication systems of marine diesel engines. Pol Marit Res 2022, vol. 29, no. 4, pp. 88–96. https://doi.org/10.2478/pomr-2022-0046

9. Qian HY. Fault characteristic analysis and diagnosis study of turbocharger rotor-bearing system. Jiangsu University of Science and Technology, 2023. DOI: 10.27171/d.cnki.ghdcc.2022.000464

10. Chunyu Z, Xinyang Q, Haiyu Q, et al. Research on fault diagnosis method of turbocharger rotor based on Hu-SVM-RFE. J Mech 2023, vol. 39, pp. 344–351. https://doi.org/10.1093/jom/ufad028

11. Pan R, Lin X. The application of support vector machine on fault diagnosis of the diesel engine exhaust gas turbocharger. 2012 International Conference on Computer Distributed Control and Intelligent Environmental Monitoring. IEEE, 2012, pp. 701–704. https://doi.org/10.1109/CDCIEM.2012.171

12. Anwarsha A, Narendiranath Babu T. Intelligent fault detection of rotating machinery using long-short-term memory (LSTM) network. International Conference on

Emerging Technologies and Intelligent Systems. Cham: Springer International Publishing, 2022, pp. 76–83. https://doi.org/10.1007/978-3-031-20429-6_8

13. Aljemely AH, Xuan J, Xu L, et al. Wise-local response convolutional neural network based on naïve Bayes theorem for rotating machinery fault classification. Appl Intell 2021, vol 51, pp. 6932–6950. https://doi.org/10.1007/s10489-021-02252-2

14. Liu Y, Xu Y, Liu J, et al. A hydraulic turbine fault diagnosis method based on synchrosqueezed wavelet transform and SE-ResNet. Water 2025, vol. 17, no. 3, p. 447. https://doi.org/ 10.3390/w17030447

15. Liang P, Deng C, Wu J, et al. Intelligent fault diagnosis of rotating machinery via wavelet transform, generative adversarial nets and convolutional neural network. Measurement 2020, vol. 159, p. 107768. https://doi.org/10.1016/j.measurement.2020.107768.

16. Qiao NG. Fault diagnosis and health prediction of high-speed train transmission system based on multi-sensor fusion. Jilin University, 2019. https://doi.org/10.27162/d.cnki.gjlin.2019.000070

17. Xu WM, Zhang YC, Liu WG, et al. Fusion of vibration signals from multiple observation points of flood discharge sluice pier based on correlation function. Journal of Yangtze River Scientific Research Institute 2015, vol. 32, no. 11, pp. 110–114.

18. Varbanets R, Minchev D, Kucherenko Y, et al. Methods of real-time parametric diagnostics for marine diesel engines. Pol Marit Res 2024, vol. 31, no. 3, pp. 71–84. https://doi.org/10.2478/pomr-2024-0037

19. Canalle GK, Salgado AC, Loscio BF. A survey on data fusion: What for? In what form? What is next? J Intell Inf Syst 2021, vol. 57, no. 1, pp. 25–50. https://doi.org/10.1007/s10844-020-00627-4

20. Yin S, Wang G, Gao H. Data-driven process monitoring based on modified orthogonal projections to latent structures. Ieee T Contr Syst T 2015, vol. 24, no. 4, pp. 1480–1487. https://doi.org/10.1109/TCST.2015.2481318

21. Puzdrowska P. Diagnostic analysis of exhaust gas with a quick-changing temperature from a marine diesel engine Part II: Two factor analysis. Pol Marit Res 2023, vol. 3, no. 7, pp. 11–17. https://doi.org/10.2478/pomr-2023-0042

22. Varbanets R, Fomin O, Píštěk V, et al. Acoustic method for estimation of marine low-speed engine turbocharger parameters. J Mar Sci Eng 2021, vol. 9, no. 3, p. 321. https://doi.org/10.3390/jmse9030321

23. Dong F, Yang J, Cai Y, et al. Transfer learning-based fault diagnosis method for marine turbochargers. Actuators 2023, vol. 12, no. 4, p. 146. https://doi.org/10.3390/act12040146

24. Dong F, Yang J, Hu L, et al. Multi-objective matched synchrosqueezing chirplet transform for fault feature extraction from marine turbochargers. IEEE Access 2023, vol. 11, pp. 80702–80715. https://doi.org/10.1109/ACCESS.2023.3296689

25. Qiao Q, Wang HJ, Ma K, et al. Gas turbine rotor fault diagnosis based on improved DenseNet-ViT joint network and transfer learning. Journal of Electronic Measurement and Instrumentation 2024, vol 38, no. 11, pp. 40-47. https://doi.org/10.13382/j.jemi.B2407526

26. Zorich VA. Entropy in thermodynamics and in information theory. Probl Inform Transm 2022, vol. 58, no. 2, pp. 103–110. https://doi.org/10.1134/S0032946022020016

27. Gour G, Tomamichel M. Entropy and relative entropy from information-theoretic principles. Ieee T Inform Theory 2021, vol. 67, no. 10, pp. 6313–6327. https://doi.org/10.1109/TIT.2021.3078337

28. Nascimento WS, Maniero AM, Prudente FV, et al. Electron confinement study in a double quantum dot by means of Shannon entropy information. Physica B 2024, vol. 677, p. 415692. https://doi.org/10.1016/j.physb.2024.415692

29. Lin J, Chen Q. Application of the EEMD method to multiple faults diagnosis of gearbox. 2010 2nd International Conference on Advanced Computer Control. IEEE, 2010, vol. 2, pp. 395–399. https://doi.org/10.1109/ICACC.2010.5486649

30. Dibaj A, Ettefagh MM, Hassannejad R, et al. A hybrid fine-tuned VMD and CNN scheme for untrained compound fault diagnosis of rotating machinery with unequal-severity faults. Expert Syst Appl 2021, vol. 167, p. 114094. https://doi.org/10.1016/j.eswa.2020.114094

31. Ni Q, Ji JC, Feng K, et al. A fault information-guided variational mode decomposition (FIVMD) method for rolling element bearings diagnosis. Mech Syst Signal Pr 2022, vol. 164, p. 108216. https://doi.org/10.1016/j.ymssp.2021.108216

32. Wang H, Zhang C, Zhao P, Yan M, Jin, Y. Gas turbine shock measurement point optimization based on shock response analysis. Journal of Vibration and Shock 2025, vol. 44, no. 4, pp. 244–252. https://doi.org/10.13465/j.cnki.jvs.2025.04.026

33. Zhang Z, Wang Z, Yu F. Optimization of vibration sensor placement for ship aft using local linear embedding. Noise

and Vibration Control 2025, vol. 45, no. 1, p. 294. https://doi.org/10.3969/j.issn.1006-1355.2025.01.046

34. Kammer DC. Sensor placement for on-orbit modal identification and correlation of large space structures. J Guid Control Dynam 1991, vol. 14, no. 2, pp. 251–259. https://doi.org/10.23919/ACC.1990.4791265

35. Greenacre M, Groenen PJF, Hastie T, et al. Principal component analysis. Nat Rev Method Prime 2022, vol. 2, no. 1, p. 100. https://doi.org/10.1038/s43586-022-00184-w

36. Gewers FL, Ferreira GR, Arruda HFD, et al. Principal component analysis: A natural approach to data exploration. Acm Comput Surv (CSUR) 2021, vol. 54, no. 4, pp. 1–34. https://doi.org/10.1145/3447755

37. Tomeo I, Markopoulos PP, Savakis A. Quantum annealing for robust principal component analysis. arXiv: 2501.10431, 2025. https://doi.org/10.48550/arXiv.2501.10431

38. Lahdhiri H, Taouali O. Reduced rank KPCA based on GLRT chart for sensor fault detection in nonlinear chemical process. Measurement 2021, vol. 169, pp. 108342. https://doi.org/10.1016/j.measurement.2020.108342

39. Zhong JH, Huang C, Zhong SC, et al. Remaining useful life of rolling bearing based on t-SNE. Journal of Mechanical Strength 2024, vol. 46, no. 04, pp. 969–976. https://doi.org/10.16579/j.issn.1001.9669.2024.04.028

40. Van der Maaten L, Hinton G. Visualizing data using t-SNE. J Mach Learn Res 2008, vol. 9, no. 11, pp. 2579–2605.

41. Liang Z, Zhang L, Wang X. A novel intelligent method for fault diagnosis of steam turbines based on T-SNE and XGBoost. Algorithms 2023, vol. 16, no. 2, p. 98. https://doi.org/_10.3390/a16020098

42. Liang K, Zhao HJ, Song WZ. Research on evaluation of internal combustion engine sound quality based on convolutional neural network. Chinese Internal Combustion Engine Engineering 2019, vol. 40, no. 02, pp. 67–75. https://doi.org/10.13949/j.cnki.nrjgc.2019.02.010

43. Zhang BW, Pang XY, Cheng BA, et al. Fault diagnosis method for aeroengine bearing based on PIRD-CNN. Journal of Vibration and Shock 2024, vol. 43, no. 18, pp. 201–207+231. https://doi.org/10.13465/j.cnki.jvs.2024.18.022

44. China Machinery Industry Federation. Intelligent Services Predictive Maintenance Algorithm Measurement Method: GB/T43555-2023. Beijing: China Standard Press, 2023.